

Dark matter, Z' , vector-like quark at the LHC and $b \rightarrow s\mu\mu$ anomaly

Wei Chao¹, Hongxin Wang², Lei Wang², Yang Zhang³

¹ *Center for Advanced Quantum Studies, Department of Physics,*

Beijing Normal University, Beijing, 100875, P. R. China

² *Department of Physics, Yantai University, Yantai 264005, P. R. China*

³ *School of Physics and Microelectronics,*

Zhengzhou University, ZhengZhou 450001, P. R. China

Abstract

In this paper, combining the $b \rightarrow s\mu^+\mu^-$ anomaly and dark matter observables, we study the capability of LHC to test dark matter, Z' , and vector-like quark. We focus on a local $U(1)_{L_\mu-L_\tau}$ model with a vector-like $SU(2)_L$ doublet quark Q and a complex singlet scalar whose lightest component X_I is a candidate of dark matter. After imposing relevant constraints, we find that the $b \rightarrow s\mu^+\mu^-$ anomaly and the relic abundance of dark matter favor $m_{X_I} < 350$ GeV and $m_{Z'} < 450$ GeV for $m_Q < 2$ TeV and $m_{X_R} < 2$ TeV (the heavy partner of m_{X_I}). The current searches for jets and missing transverse momentum at the LHC sizably reduce the mass ranges of the vector-like quark, and m_Q is required to be larger than 1.7 TeV. Finally, we discuss the possibility of probing these new particles at the high luminosity LHC via the QCD process $pp \rightarrow D\bar{D}$ or $pp \rightarrow U\bar{U}$ followed by the decay $D \rightarrow s(b)Z'X_I$ or $U \rightarrow u(c)Z'X_I$ and then $Z' \rightarrow \mu^+\mu^-$. Taking a benchmark point of $m_Q=1.93$ TeV, $m_{Z'} = 170$ GeV, and $m_{X_I} = 145$ GeV, we perform a detailed Monte Carlo simulation, and find that such benchmark point can be accessible at the 14 TeV LHC with an integrated luminosity 3000 fb^{-1} .

I. INTRODUCTION

At present, there are several interesting excesses in B -physics measurements involving the transition $b \rightarrow s\ell^+\ell^-$ ($\ell = \mu, e$),

$$R_{K^{(*)}} \equiv \frac{B \rightarrow K^{(*)}\mu^+\mu^-}{B \rightarrow K^{(*)}e^+e^-}. \quad (1)$$

The LHCb results for the R_K ratio in one q_2 bin [1, 2] and the R_{K^*} ratio in two q_2 bins [3] were found to lie significantly below one:

$$\begin{aligned} R_K &= 0.846_{-0.054}^{+0.060}(\text{stat})_{-0.014}^{+0.016}(\text{syst}), & q^2 \in [1, 6] \text{ GeV}^2, \\ R_{K^*} &= 0.660_{-0.070}^{+0.110}(\text{stat}) \pm 0.024(\text{syst}), & q^2 \in [0.045, 1.1] \text{ GeV}^2, \\ R_{K^*} &= 0.685_{-0.069}^{+0.113}(\text{stat}) \pm 0.047(\text{syst}), & q^2 \in [1.1, 6.0] \text{ GeV}^2. \end{aligned} \quad (2)$$

Belle announced its measurement of R_{K^*} [4]

$$R_{K^*} = \begin{cases} 0.52_{-0.26}^{+0.36} \pm 0.05, & 0.045 \leq q^2 \leq 1.1 \text{ GeV}^2, \\ 0.96_{-0.29}^{+0.45} \pm 0.11, & 1.1 \leq q^2 \leq 6.0 \text{ GeV}^2, \\ 0.90_{-0.21}^{+0.27} \pm 0.10, & 0.1 \leq q^2 \leq 8.0 \text{ GeV}^2, \\ 1.18_{-0.32}^{+0.52} \pm 0.10, & 15.0 \leq q^2 \leq 19.0 \text{ GeV}^2, \\ 0.94_{-0.14}^{+0.17} \pm 0.08, & 0.045 \leq q^2. \end{cases} \quad (3)$$

The global fits to the experimental data show the new physics (NP) model can explain the anomalies of $R(K)$ and $R(K^*)$ by contributing to C_9^μ . With $C_{10}^{\mu, NP} = 0$, the best fit value for $C_9^{\mu, NP}$ is -1.10 ± 0.16 [5].

A $U(1)_{L_\mu-L_\tau}$ gauge boson couples only to $\mu(\tau)$ but not to electron [6], and this type of $U(1)_{L_\mu-L_\tau}$ model has also been modified from its minimal version to explain $b \rightarrow s\mu^+\mu^-$ anomaly [7–23]. In Ref. [23], in addition to the $U(1)_{L_\mu-L_\tau}$ gauge boson Z' and a complex singlet \mathcal{S} breaking $U(1)_{L_\mu-L_\tau}$ symmetry, a vector-like $SU(2)_L$ doublet quark Q and a complex singlet X are introduced to produce the $Z'bs$ coupling large enough to explain the anomalies of $R(K^{(*)})$. As the lightest component of X , X_I is a candidate of dark matter (DM). In this paper, we will combine the $b \rightarrow s\mu^+\mu^-$ anomaly and the experimental data of DM, and study the capability of LHC to test dark matter, Z' , and vector-like quark.

TABLE I: The quantum numbers of the vector-like quark $Q \equiv (U, D)$, the scalars X and S under the gauge group $SU(3)_C \times SU(2)_L \times U(1)_Y \times U(1)_{L_\mu-L_\tau}$.

	$SU(3)_c$	$SU(2)_L$	$U(1)_Y$	$U(1)_{B-L}$
Q	3	2	$+1/6$	$-q_x$
X	1	1	0	q_x
S	1	1	0	$-2q_x$

Our work is organized as follows. In Sec. II we recapitulate the model. In Sec. III we consider the relevant theoretical constraints and $b \rightarrow s$ flavor observables, and explain the $b \rightarrow s\mu^+\mu^-$ anomaly. In Sec. IV, we discuss the DM observables. In Sec. V, we use the current searches at the LHC to constrain the parameter space, and analyze the possibility of probing the new particles at the high luminosity LHC. Finally, we give our conclusion in Sec. VI.

II. THE MODEL

In addition to the $U(1)_{L_\mu-L_\tau}$ gauge boson Z' , the model predicts a complex singlet S , a complex singlet X , and a $SU(2)_L$ doublet quark Q . Their quantum numbers under the gauge group $SU(3)_C \times SU(2)_L \times U(1)_Y \times U(1)_{L_\mu-L_\tau}$ are shown in Table I.

The Lagrangian which remains invariant under the $SU(3)_C \times SU(2)_L \times U(1)_Y \times U(1)_{L_\mu-L_\tau}$ symmetry is given by

$$\begin{aligned}
\mathcal{L} = & \mathcal{L}_{\text{SM}} - \frac{1}{4}Z'_{\mu\nu}Z'^{\mu\nu} + g_{Z'}Z'^\mu(\bar{\mu}\gamma_\mu\mu + \bar{\nu}_{\mu L}\gamma_\mu\nu_{\mu L} - \bar{\tau}\gamma_\mu\tau - \bar{\nu}_{\tau L}\gamma_\mu\nu_{\tau L}) \\
& - V + \bar{Q}(i\not{D} - M_Q)Q \\
& + (D_\mu X^\dagger)(D^\mu X) + (D_\mu S^\dagger)(D^\mu S) - \sum_{i=1}^3(\lambda_i \bar{q}_L^i Q X + h.c.).
\end{aligned} \tag{4}$$

Where we ignore the kinetic mixing term of gauge bosons of $U(1)_{L_\mu-L_\tau}$ and $U(1)_Y$. q_L^i denotes the SM left-handed quark doublet with $i = 1, 2, 3$, and D_μ is the covariant derivative. The field strength tensor $Z'_{\mu\nu} = \partial_\mu Z'_\nu - \partial_\nu Z'_\mu$, and $g_{Z'}$ is the gauge coupling constant of the

$U(1)_{L_\mu-L_\tau}$ group. The scalar potential V is given by

$$\begin{aligned} V = & -\mu_h^2(H^\dagger H) - \mu_S^2(\mathcal{S}^\dagger \mathcal{S}) + m_X^2(X^\dagger X) + [\mu X^2 \mathcal{S} + \text{h.c.}] \\ & + \lambda_H(H^\dagger H)^2 + \lambda_S(\mathcal{S}^\dagger \mathcal{S})^2 + \lambda_X(X^\dagger X)^2 + \lambda_{SX}(\mathcal{S}^\dagger \mathcal{S})(X^\dagger X) \\ & + \lambda_{HS}(H^\dagger H)(\mathcal{S}^\dagger \mathcal{S}) + \lambda_{HX}(H^\dagger H)(X^\dagger X). \end{aligned} \quad (5)$$

The SM Higgs doublet H , the singlet field \mathcal{S} and X is expressed by

$$H = \begin{pmatrix} G^+ \\ \frac{1}{\sqrt{2}}(h_1 + v_h + iG) \end{pmatrix}, \mathcal{S} = \frac{1}{\sqrt{2}}(h_2 + v_S + i\omega), X = \frac{1}{\sqrt{2}}(X_R + iX_I), \quad (6)$$

Where $v_h = 246$ GeV and v_S are respectively vacuum expectation values (VeVs) of H and \mathcal{S} , and the X field has no VeV. The mass parameters μ_h^2 and μ_S^2 in the potential of Eq. (5) are determined by the potential minimization conditions,

$$\begin{aligned} \mu_h^2 &= \lambda_H v_h^2 + \frac{1}{2} \lambda_{HS} v_S^2, \\ \mu_S^2 &= \lambda_S v_S^2 + \frac{1}{2} \lambda_{HS} v_h^2. \end{aligned} \quad (7)$$

After \mathcal{S} acquires the VeV, the μ term makes the complex scalar X split into two real scalar fields X_R, X_I , and their masses are given by

$$\begin{aligned} m_{X_R}^2 &= m_X^2 + \frac{1}{2} \lambda_{HX} v_H^2 + \frac{1}{2} \lambda_{SX} v_S^2 + \sqrt{2} \mu v_S \\ m_{X_I}^2 &= m_X^2 + \frac{1}{2} \lambda_{HX} v_H^2 + \frac{1}{2} \lambda_{SX} v_S^2 - \sqrt{2} \mu v_S. \end{aligned} \quad (8)$$

The discrete Z_2 symmetry of the scalar potential in Eq. (5) makes the lightest component X to be as a candidate of DM, which we assume is X_I .

The two physical CP-even states h and S are from the mixing of h_1 and h_2 by the following relation,

$$\begin{pmatrix} h_1 \\ h_2 \end{pmatrix} = \begin{pmatrix} \cos \theta & \sin \theta \\ -\sin \theta & \cos \theta \end{pmatrix} \begin{pmatrix} h \\ S \end{pmatrix}, \quad (9)$$

where θ is the mixing angle. The two CP-even Higgses mediate the DM interactions,

$$\begin{aligned} \mathcal{L}(X_I X_I, h, S) = & -\frac{1}{2} [\lambda_{HX} v_H c_\theta - (\lambda_{SX} v_S - \sqrt{2} \mu) s_\theta] h X_I^2 \\ & -\frac{1}{2} [\lambda_{HX} v_H s_\theta + (\lambda_{SX} v_S - \sqrt{2} \mu) c_\theta] S X_I^2. \end{aligned} \quad (10)$$

In this paper, in order to suppress the stringent constraints from the DM direct detection and indirect detection experiments, we simply assume the $hX_I X_I$ coupling is absent, namely taking $\theta = 0$ and $\lambda_{HX} = 0$. For $\theta = 0$, we obtain the following expressions,

$$\lambda_{HS} = 0, \quad \lambda_H = \frac{m_h^2}{2v_h^2}, \quad \lambda_S = \frac{m_S^2}{2v_S^2}. \quad (11)$$

After \mathcal{S} gets VEV, the $U(1)_{L_\mu-L_\tau}$ gauge boson Z' obtains a mass,

$$m'_Z = 2g'_Z |q_x| v_S. \quad (12)$$

The complex singlet X mediates the new Yukawa interactions of the vector-like quarks and the SM left-handed quark,

$$\Delta\mathcal{L}_{\text{Yukawa}} = -\frac{1}{\sqrt{2}} \sum_{i=1,2,3} (\lambda_{u_i} \bar{u}_{iL} U + \lambda_{d_i} \bar{d}_{iL} D) (X_R + iX_I) + h.c., \quad (13)$$

where we assume that the down-type quarks are already in the mass basis, and rotate the interaction eigenstates of up-type quarks to the mass eigenstates via the CKM matrix V . Thus, $\lambda_{u_i} \equiv \sum_j V_{ij} \lambda_j$ and $\lambda_{d_i} \equiv \lambda_i$ with $u_i = u, c, t$ and $d_i = d, s, b$. We will simply set $\lambda_1 = 0$ to remove the constraints related to the first generation quarks. As a result, λ_u is much smaller than λ_c and λ_t due to the suppression of the factors of V_{us} and V_{ub} .

III. $b \rightarrow s\mu^+\mu^-$ ANOMALY

We apply the upper bound of $g_{Z'}/m_{Z'} \leq (550 \text{ GeV})^{-1}$ from the neutrino trident process [24], and require $g_{Z'} q_x \leq 1$ to maintain the perturbativity of the Z' couplings. The tree-level stability of the potential of Eq. (5) requires

$$\begin{aligned} \lambda_H &\geq 0, \quad \lambda_S \geq 0, \quad \lambda_X \geq 0, \\ \lambda_{HS} &\geq -2\sqrt{\lambda_H \lambda_S}, \quad \lambda_{HX} \geq -2\sqrt{\lambda_H \lambda_X}, \quad \lambda_{SX} \geq -2\sqrt{\lambda_S \lambda_X}, \\ &\sqrt{\lambda_{HS} + 2\sqrt{\lambda_H \lambda_S}} \sqrt{\lambda_{HX} + 2\sqrt{\lambda_H \lambda_X}} \sqrt{\lambda_{SX} + 2\sqrt{\lambda_S \lambda_X}} \\ &+ 2\sqrt{\lambda_H \lambda_S \lambda_X} + \lambda_{HS}\sqrt{\lambda_X} + \lambda_{HX}\sqrt{\lambda_S} + \lambda_{SX}\sqrt{\lambda_H} \geq 0. \end{aligned} \quad (14)$$

We scan over the other parameters in the following ranges:

$$\begin{aligned} 60\text{GeV} &\leq m_{X_I} \leq 1\text{TeV}, \quad 800\text{GeV} \leq m_{X_R} \leq 2\text{TeV}, \quad 1\text{TeV} \leq m_Q \leq 2\text{TeV}, \\ 100\text{GeV} &\leq m_{Z'} \leq 1000\text{GeV}, \quad 100\text{GeV} \leq m_S \leq 1000\text{GeV}, \\ 0.1 &\leq \lambda_{bs} (\equiv \lambda_b \lambda_s) < 0.3 \text{ with } \lambda_{b,s} \leq 1. \end{aligned} \quad (15)$$

We consider four relevant $b \rightarrow s$ flavor observables, $R_{K^{(*)}}$, Δm_s , $B \rightarrow X_s \gamma$, and $R_{K^{(*)}}^{\nu\nu}$, which are introduced in detail in Ref. [23]. Here we give the expressions for calculating the four observables briefly.

A. Numerical calculations

I. $R_{K^{(*)}}$ anomalies

The model does not contain the tree-level Z' - b - s flavor-changing coupling, but produces the Z' - b - s coupling via the one-loop involving the vector-like quarks, X_R and X_I . The $b \rightarrow s \mu^+ \mu^-$ transition operator O_9^μ is generated by Z' -exchanging penguin diagrams. The corresponding Wilson coefficient $C_9^{\mu, NP}$ is given by [23],

$$C_9^{\mu, NP} = -\frac{\sqrt{2}q_x}{8G_F m_{Z'}^2} \frac{\alpha_{Z'}}{\alpha_{\text{em}}} \frac{\lambda_s \lambda_b^*}{V_{ts}^* V_{tb}} \left[\frac{1}{2} (k'(x_I) + k'(x_R)) - k(x_I, x_R) \right], \quad (16)$$

where $x_{R,I} = m_{X_{R,I}}^2/m_Q^2$,

$$k(x) = \frac{x^2 \log x}{x-1}, \quad k(x_1, x_2) = \frac{k(x_1) - k(x_2)}{x_1 - x_2}. \quad (17)$$

The prime on the k functions denotes a derivative with respect to the argument. A large mass splitting between m_{X_R} and m_{X_I} can enhance the absolute value of $C_9^{\mu, NP}$ which can explain $R_{K^{(*)}}$ anomaly.

II. Δm_s for $B_s - \bar{B}_s$ mixing, $B \rightarrow X_s \gamma$, and $R_{K^{(*)}}^{\nu\nu}$

The model gives the new contributions to $B_s - \bar{B}_s$ mixing via the box diagrams involving the vector-like quarks, X_R and X_I , which can be written in the form

$$H_{eff}^{\Delta B=2, NP} = C_1^{NP} (\bar{s} \gamma_\mu P_L b) (\bar{s} \gamma^\mu P_L b). \quad (18)$$

Where C_1^{NP} is given as [23]

$$C_1^{NP} = \frac{(\lambda_s \lambda_b^*)^2}{128 \pi^2 M_D^2} k(1, x_R, x_I), \quad (19)$$

where

$$k(1, x_R, x_I) = \frac{k(1, x_I) - k(x_R, x_I)}{1 - x_R}. \quad (20)$$

At the 2σ confidence level, the measurement of the mass difference in the $B_s - \bar{B}_s$ system gives a constraint on the value of C_1^{NP} [13],

$$-2.1 \times 10^{-11} \leq C_1^{NP} \leq 0.6 \times 10^{-11} (\text{GeV}^{-2}). \quad (21)$$

The model gives the new contributions to $B \rightarrow X_s \gamma$ via the one-loop diagram involving the vector-like quarks, X_R and X_I . The Wilson coefficients $C_{7\gamma, 8g}$ is corrected [23],

$$\begin{aligned} C_{7\gamma}^{\text{NP}} &= \frac{\sqrt{2}}{48} \frac{\lambda_s \lambda_b^*}{V_{ts}^* V_{tb}} \frac{1}{G_F M_D^2} (J_1(x_I) + J_1(x_R)), \\ C_{8g}^{\text{NP}} &= -\frac{\sqrt{2}}{16} \frac{\lambda_s \lambda_b^*}{V_{ts}^* V_{tb}} \frac{1}{G_F M_D^2} (J_1(x_I) + J_1(x_R)), \end{aligned} \quad (22)$$

where

$$J_1(x) = \frac{1 - 6x + 3x^2 + 2x^3 - 6x^2 \log x}{12(1-x)^4}. \quad (23)$$

The experimental measurement of the inclusive branching fraction of $B \rightarrow X_s \gamma$ is $(3.32 \pm 0.15) \times 10^{-4}$ [25], and the SM prediction is $(3.36 \pm 0.23) \times 10^{-4}$ [26]. The explanation of experimental values at 2σ level requires

$$-6.3 \times 10^{-2} \leq C_{7\gamma}^{\text{NP}} + 0.24 C_{8g}^{\text{NP}} \leq 7.3 \times 10^{-2}. \quad (24)$$

The model gives the additional contributions to $B \rightarrow K^{(*)} \nu \bar{\nu}$ via the diagrams which are obtained by replacing the external muon lines of the $b \rightarrow s \mu^+ \mu^-$ diagrams with the neutrino lines. The current experimental bounds are

$$R_K^{\nu \bar{\nu}} < 4.3, \quad R_{K^*}^{\nu \bar{\nu}} < 4.4, \quad (\text{at } 90\% \text{ C.L.}). \quad (25)$$

with

$$R_{K^{(*)}}^{\nu \bar{\nu}} = \frac{\mathcal{B}(B \rightarrow K^{(*)} \nu \bar{\nu})^{\text{exp}}}{\mathcal{B}(B \rightarrow K^{(*)} \nu \bar{\nu})^{\text{SM}}}. \quad (26)$$

In the model, the prediction value of $R_{K^{(*)}}^{\nu \bar{\nu}}$ is [23]

$$R_{K^{(*)}}^{\nu \bar{\nu}} = \frac{\sum_{i=1}^3 |C_L^{\text{SM}} + C_L^{ii, \text{NP}}|^2}{3 |C_L^{\text{SM}}|^2} = 1 + \frac{2 |C_L^{22, \text{NP}}|^2}{3 |C_L^{\text{SM}}|^2}, \quad (27)$$

with $C_L^{\text{SM}} \approx -6.35$, $C_L^{11, \text{NP}} = 0$, and

$$C_L^{22, \text{NP}} = -C_L^{33, \text{NP}} = -\frac{\sqrt{2} q_x}{16 G_F m_{Z'}^2} \frac{\alpha_{Z'}}{\alpha_{\text{em}}} \frac{\lambda_s \lambda_b^*}{V_{ts}^* V_{tb}} \left[\frac{1}{2} (k'(x_I) + k'(x_R)) - k(x_I, x_R) \right]. \quad (28)$$

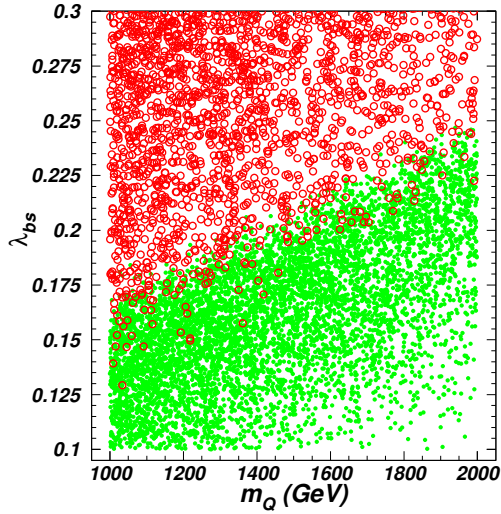


FIG. 1: The surviving samples projected on the planes of m_Q versus λ_{bs} . All the samples accommodate the $R_{K^{(*)}}$ anomaly, and the bullets (green) and circles (red) are respectively allowed and excluded by the Δm_s .

B. Results and discussions

After imposing the constraints mentioned above, we use the model to explain the $R_{K^{(*)}}$ anomalies. The bounds of $B \rightarrow X_s \gamma$ and $R_{K^{(*)}}^{\nu\nu}$ are almost satisfied in the whole parameter space being consistent with $R_{K^{(*)}}$. However, there is a strong correlation between Δm_s and $R_{K^{(*)}}$, as shown in the Eq. (16) and Eq. (19). Fig. 1 shows that $R_{K^{(*)}}$ are explained in the whole region of $1000 \text{ GeV} \leq m_Q \leq 2000 \text{ GeV}$ and $0.1 \leq \lambda_{bs} \leq 0.3$. However, Δm_s imposes an upper bound on λ_{bs} , which increases with m_Q . Due to the constraints of Δm_s , the $R_{K^{(*)}}$ anomaly can be only explained in the region of $\lambda_{bs} \leq 0.25$.

After imposing the relevant $b \rightarrow s$ flavor observables, the neutrino trident process, and the theoretical constraints, the samples explaining the $R_{K^{(*)}}$ anomaly are projected on the Fig. 2. The left panel shows that the parameters $g_{Z'q_X}$ and $m_{Z'}$ are imposed strong constraints. Due to the constraints of the neutrino trident process, the region with small $m_{Z'}$ and large $g_{Z'q_X}$ is empty. To accommodate the $R_{K^{(*)}}$ anomaly, $m_{Z'}$ is required to increase with $g_{Z'q_X}$. Since we take $g_{Z'q_x} \leq 1$ to maintain the perturbativity of the Z' couplings, $m_{Z'} > 600 \text{ GeV}$ is excluded. Similarly, $g_{Z'q_x} \leq 0.2$ is disfavored since the minimal value of $m_{Z'}$ is taken as 100 GeV .

The right panel of Fig. 2 shows that m_{X_I} is required to increase with m_{X_R} since a sizable

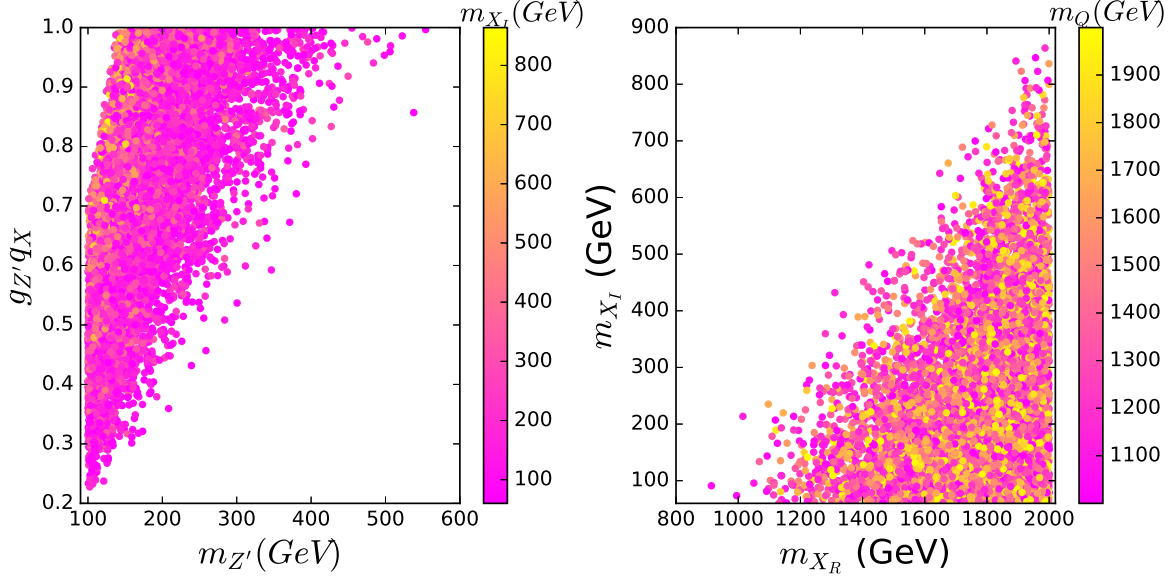


FIG. 2: All the samples accomodate the $R_{K^{(*)}}$ anomaly, and satisfy the relevant $b \rightarrow s$ flavor observables, the neutrino trident process, and the theoretical constraints.

mass splitting between m_{X_R} and m_{X_I} is favoured to explain the $R_{K^{(*)}}$ anomaly. Because we choose $m_{X_R} \leq 2$ TeV, m_{X_I} is required to be smaller than 900 GeV. Similarly, $m_{X_R} \leq 800$ GeV is disfavored since the minimal value of m_{X_I} is taken as 60 GeV.

IV. DARK MATTER

In the chosen parameter space, the DM can annihilation into $Z'Z'$, SS , and the SM quarks. The corresponding Feynman diagrams are shown in the Fig. 3. The $X_I X_I \rightarrow q\bar{q}$ processes proceed through the $D(U)$ -exchanging t-channel diagrams. For $1 \text{ TeV} \leq m_Q \leq 2 \text{ TeV}$, $\lambda_b < 1$, and $\lambda_s < 1$, the annihilation cross sections are very small, and their contributions to the relic density can be ignored. The $X_I X_I \rightarrow SS$ processes proceed through the S -exchanging s-channel diagram and the diagram of the quartic coupling $X_I X_I SS$. The $X_I X_I \rightarrow Z'Z'$ proceed through the S -exchanging s-channel diagram, the X_R -exchanging t-channel diagram, and the diagram of the quartic coupling $X_I X_I Z'Z'$.

We use `micrOMEGAs` [27] to calculate the relic density and the spin-independent DM-nucleon cross section. The model file is generated by `FeynRules` [28]. The Planck collaboration reported the relic density of cold DM in the universe, $\Omega_c h^2 = 0.1198 \pm 0.0015$ [29].

The annihilation cross section of $X_I X_I \rightarrow Z'Z'$ from the diagram of Fig. 3(c) only

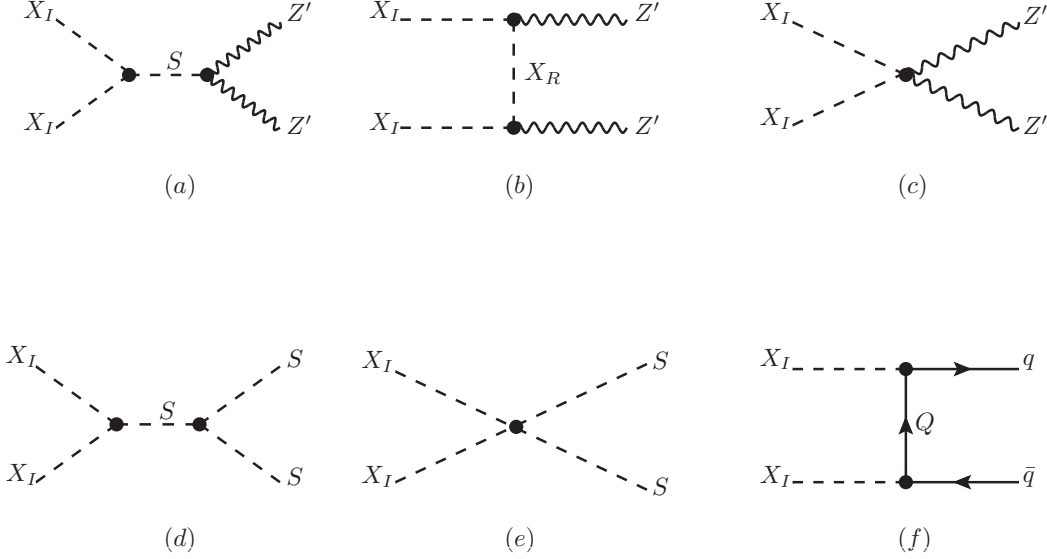


FIG. 3: The Feynman diagrams for $X_I X_I \rightarrow Z' Z', SS, q\bar{q}$.

depends on three parameters $g_{Z'} q_X, m_{Z'}, m_{X_I}$. Since the $R_{K(*)}$ anomaly imposes a lower bound on $g_{Z'} q_X$, for $m_{Z'} < m_{X_I}$ the annihilation cross sections of $X_I X_I \rightarrow Z' Z'$ are much larger than the value producing the correct relic density. Similarly, for $m_S < m_{X_I}$ the annihilation cross sections of $X_I X_I \rightarrow SS$ are too large to obtain the correct relic density. Therefore, we need to use the effects of forbidden channel to produce the relic density, namely that $m_{Z'}$ or m_S is appropriately larger than m_{X_I} . In the calculation of the thermal averaged cross section, the kinetic energy of the DM is nonnegligible in the early universe. When the mass difference is not too large and the DMs move fast, the center of mass energy exceeds twice $m_{Z'}$ or m_S . Therefore, the process $X_I X_I \rightarrow Z' Z' (SS)$ can occur in the early universe when m_{X_I} has appropriate mass difference from $m_{Z'} (m_S)$. In addition, the temperature at the present time is much lower than the freeze-out temperature, and the velocity of DM is much smaller than that in the early universe. The channel $X_I X_I \rightarrow Z' Z' (SS)$ are kinematically forbidden at the present time, therefore the experimental constraints of the indirect detection of DM can be naturally satisfied.

After imposing the constraints of "pre-DM" (denoting the $R_{K(*)}$ anomaly, the relevant $b \rightarrow s$ flavor observables, the neutrino trident process, and the theoretical constraints), we

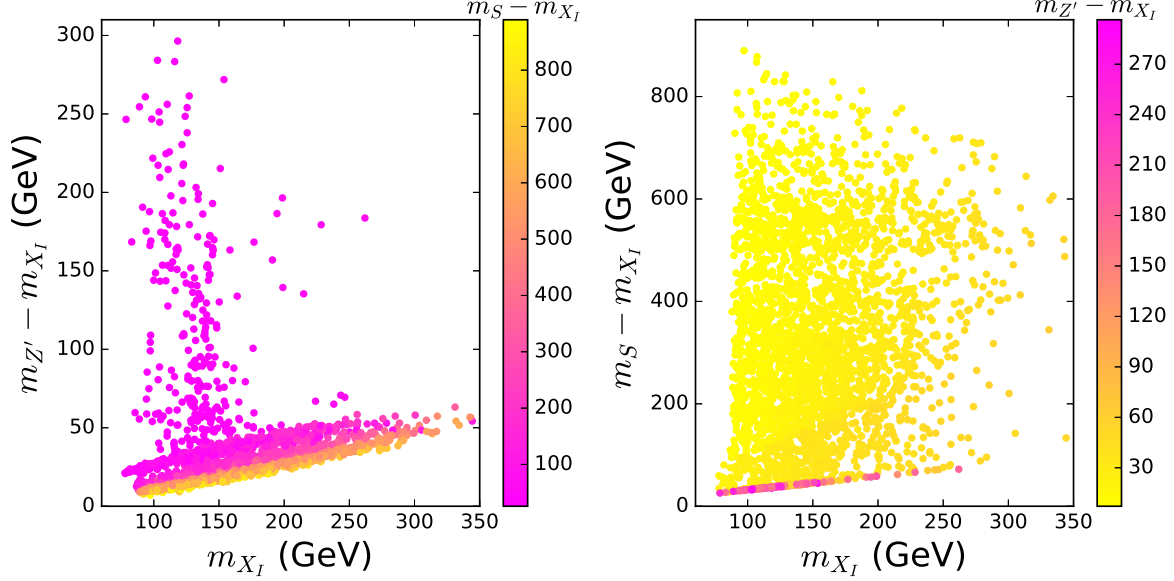


FIG. 4: The surviving samples satisfying the DM relic density and the constraints of "pre-DM".

find some samples which can achieve the correct DM relic density. The surviving samples are project on the Fig. 4. From the left panel, we find that the relic density favors $m_{X_I} < 350$ GeV, and most of the surviving samples lie in the region of $m_{Z'} - m_{X_I} < 60$ GeV. For a large m_S , the annihilation cross section of $X_I X_I \rightarrow Z' Z'$ from the diagram of Fig. 3(a) is suppressed. Therefore, a small value of $m_{Z'} - m_{X_I}$ is required to enhance the cross section. For a large value of $m_{Z'} - m_{X_I}$, the $X_I X_I \rightarrow Z' Z'$ channel is still forbidden in the early universe, and does not contribute to the relic density. For such case, the $X_I X_I \rightarrow SS$ channel will play the dominant contribution to the relic density. As shown in the right panel, for a large value of $m_{Z'} - m_{X_I}$, a small value of $m_S - m_{X_I}$ is required to open the $X_I X_I \rightarrow SS$ channel in the early universe.

Exchanging an initial state X_I and a final state quark of Fig. 3(f), we can obtain the Feynman diagrams which give the contributions to the cross section of the DM scattering off the nuclei. In the chosen parameter space, we find that the bounds of the XENON1T fail to exclude the parameter space achieving the correct relic density [30].

V. THE DARK MATTER, Z' , AND VECTOR-LIKE QUARK AT THE LHC

A. The current constraints from the direct searches at the LHC

At the LHC, the vector-like quarks D and U are produced in pairs via the QCD processes,

$$pp \rightarrow D\bar{D}, U\bar{U}. \quad (29)$$

In the chosen parameter space, the D and U have following decay modes,

$$D \rightarrow X_I d_i, X_R d_i, \quad U \rightarrow X_I u_i, X_R u_i \quad (30)$$

with

$$X_R \rightarrow X_I Z' \rightarrow X_I \mu^+ \mu^-, X_I \tau^+ \tau^-, X_I \nu_\mu \bar{\nu}_\mu, X_I \nu_\tau \bar{\nu}_\tau. \quad (31)$$

Since the $R_{K^{(*)}}$ anomaly and the DM relic density favor X_R to be much larger than X_I , D and U will mainly decay into $X_I s$, $X_I b$, and $X_I u_i$. In this paper, the coupling of X_I and d quark is taken as zero.

In order to restrict the productions of the above processes at the LHC for our model, we perform simulations for the samples using **MG5_aMC-2.7.3** [31] with **PYTHIA8** [32] and **Delphes-3.2.0** [33], and adopt the constraints from all the analysis for the 13 TeV LHC in version **CheckMATE 2.0.28** [34]. For the excluded samples, the most sensitive experimental analysis is the ATLAS search for the squarks and gluinos in final states containing jets and missing transverse momentum at 13 TeV LHC with 139 fb⁻¹ integrated luminosity data [35]. The final states $E_T^{miss} + jets$ are just the main signal of the $D\bar{D}$ and $U\bar{U}$ in the model.

In Fig. 5, all the samples satisfy the constraints of "pre-DM" and the DM observables. The current direct searches at the LHC exclude $m_Q < 1.7$ TeV. For a large λ_s , some samples with m_Q around 1.8 TeV can be also excluded. With an increase of m_Q , the production cross sections of $pp \rightarrow D\bar{D}$, $U\bar{U}$ are suppressed by the phase space, and the direct searches at the LHC can be satisfied.

B. The searches for the new particles at the high luminosity LHC

Since the vector-like quark U and D are charged under the $U(1)_{L_\mu - L_\tau}$, the gauge boson Z' has the tree-level couplings to the vector-like quarks. Therefore, the model provides a

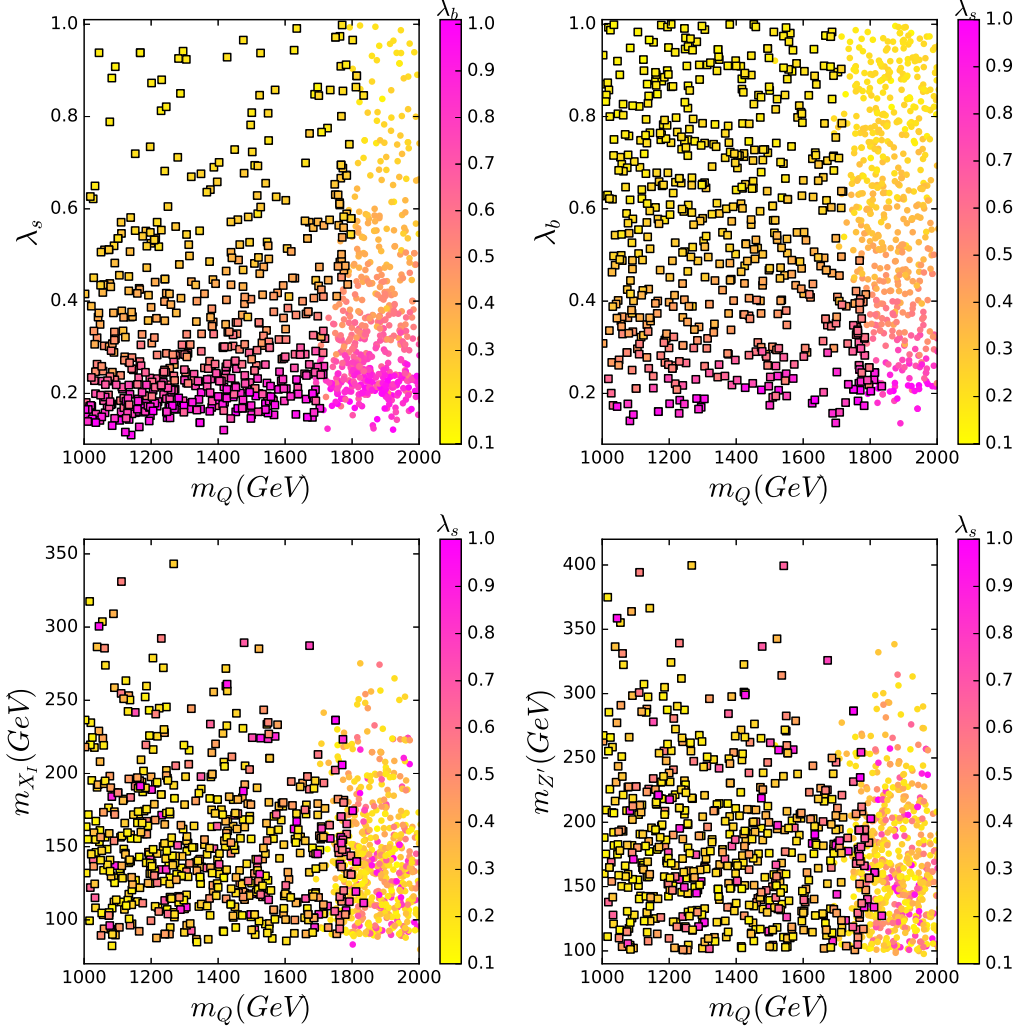


FIG. 5: All the samples satisfy the constraints of "pre-DM" and the DM observables. The squares and bullets are respectively excluded and allowed by the current direct searches at the LHC.

novel approach of searching for Z' , the vector-like quark, and DM. Z' is produced via the QCD process $pp \rightarrow D\bar{D}$ or $pp \rightarrow U\bar{U}$ followed by the decay $D \rightarrow s(b)X_R \rightarrow s(b)Z'X_I$ or $U \rightarrow u(c)X_R \rightarrow u(c)Z'X_I$, and then decays into $\mu^+\mu^-$.

We pick a benchmark point which accomodates the $b \rightarrow s\mu^+\mu^-$ anomaly, and satisfies the constraints of "pre-DM", the DM observables, and the current searches at the LHC. Several key input and output parameters are shown in Table II.

Now we perform detailed simulations on the signal and backgrounds at the 14 TeV LHC with high luminosity. We choose the signal to contain opposite sign di-muon ($\mu^+\mu^-$), missing transverse momentum E_T^{miss} , and multijet (≥ 2 jets) which include at least one b -jet. The major SM irreducible background processes to this signal are $t\bar{t}$, WW + jets, ZZ + jets, and

$m_{Z'}(\text{GeV})$	$m_{X_I}(\text{GeV})$	$m_{X_R}(\text{GeV})$	$m_Q(\text{GeV})$	$Br(D \rightarrow X_I b)$	$Br(D \rightarrow X_I s)$	$Br(D \rightarrow X_R b)$	$Br(D \rightarrow X_R s)$
170	145	1309	1930	0.63	0.14	0.19	0.04

TABLE II: Several key input and output parameters for the benchmark point.

$WZ + \text{jets}$.

We identify the muon candidates by requiring them to have $p_T > 15$ GeV and $|\eta| < 2.5$. The anti-kt algorithm is employed to reconstruct the jets with a radius parameter $R = 0.4$ [36], and the jets are required to have $p_T > 20$ GeV and $|\eta| < 2.5$. We assume an average b -tagging efficiency of 80% for real b -jets.

In order to suppress the contributions from the SM process, we apply the "stransverse" mass, m_{T2} [37–39], defined as

$$m_{T2} = \min_{\mathbf{q}_T} [\max(m_T(\mathbf{p}_T^{\ell_1}, \mathbf{q}_T), m_T(\mathbf{p}_T^{\ell_2}, \mathbf{p}_T^{\text{miss}} - \mathbf{q}_T))] \quad (32)$$

where $\mathbf{p}_T^{\ell_1}$ and $\mathbf{p}_T^{\ell_2}$ are the transverse momenta of the di-muon. \mathbf{q}_T is a transverse vector that minimizes the larger of the two transverse masses m_T ,

$$m_T(\mathbf{p}_T, \mathbf{q}_T) = \sqrt{2(p_T q_T - \mathbf{p}_T \cdot \mathbf{q}_T)}. \quad (33)$$

Fig. 6 shows the distributions of some kinematical variables at the LHC with $\sqrt{s} = 14$ TeV for the signal and the background $t\bar{t}$. The other processes are not shown since they are subdominant. According to the distribution differences between the signal and backgrounds, we can improve the ratio of signal to backgrounds by making some kinematical cuts. We impose the following cuts

$$\begin{aligned} P_T^{j_1} &> 290 \text{ GeV}, \quad P_T^{j_2} > 60 \text{ GeV}, \quad P_T^{b_1} > 60 \text{ GeV}, \\ \Delta R_{\mu^+ \mu^-} &< 2.0, \quad 150 \text{ GeV} < M_{\mu^+ \mu^-} < 180 \text{ GeV}, \\ E_T^{\text{miss}} &> 310 \text{ GeV}, \quad m_{T2} > 100 \text{ GeV}, \quad H_T^{b\ell} > 500 \text{ GeV}. \end{aligned} \quad (34)$$

Where $P_T^{j_1}$ and $P_T^{j_2}$ denote the transverse momentum of the hardest and the second hardest jets which include b -jet, and $P_T^{b_1}$ denotes the transverse momentum of the hardest b -jet. $\Delta R = \sqrt{(\Delta\phi)^2 + (\Delta\eta)^2}$ is the particle separation with $\Delta\phi$ and $\Delta\eta$ being the separation in the azimuthal angle and rapidity respectively. $M_{\mu^+ \mu^-}$ is the invariant mass of μ^+ and μ^- , and $H_T^{b\ell}$ is scalar sum of transverse momenta of all the b -jets, μ^\pm . Since μ^+ and μ^- of

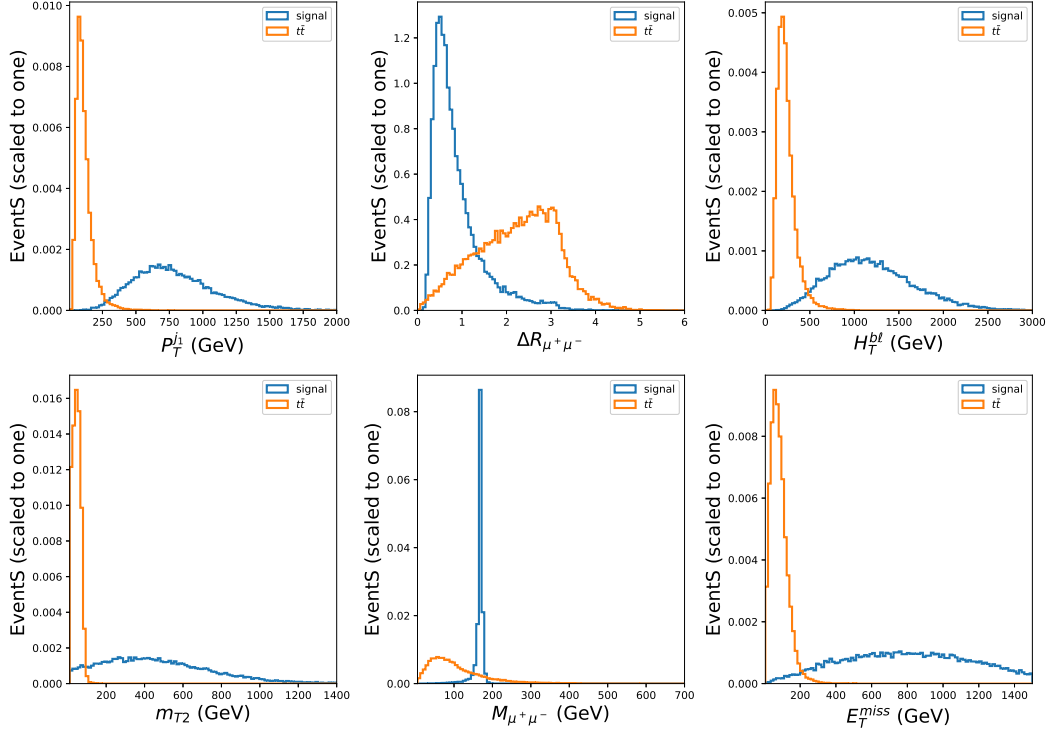


FIG. 6: The signal and the $t\bar{t}$ background distributions of P_T^{j1} , $\Delta R_{\mu^+\mu^-}$, $H_T^{b\ell}$, m_{T2} , $M_{\mu^+\mu^-}$, and E_T^{miss} at the 14 TeV LHC, after requiring an opposite sign di-muon and multijet (≥ 2 jets) which include at least one b -jet.

the signal are from the decay of Z' with a mass of 170 GeV, $M_{\mu^+\mu^-}$ appears a peak at 170 GeV, and $\Delta R_{\mu^+\mu^-}$ favors a small value. The jets, X_I and μ^\pm of the signal are the decay products of the vector-like quark with a mass of 1930 GeV, and such heavy mass leads that these products tend to have large transverse momentums. The distributions of m_{T2} for $t\bar{t}$ and WW +jets backgrounds peak before m_W . In addition, the DM X_I has a mass of 145 GeV, therefore the signal events tend to have a large E_T^{miss} .

We compute the significance as $\mathbf{S} = \frac{n_s}{\sqrt{n_s+n_b}}$, where n_s and n_b are the normalized signal and background event yields, respectively. After making the kinematical cuts of Eq. (34), n_b is drastically reduced, and dominated over by n_s . For example, $n_s \sim 33$ and $n_s + n_b \sim 35$ for a dataset 3000 fb^{-1} at the 14 TeV LHC. Fig. 7 shows that for the benchmark point, the significance can reach 2σ and 5.6σ at the 14 TeV LHC with an integrated luminosity 400 fb^{-1} and 3000 fb^{-1} .

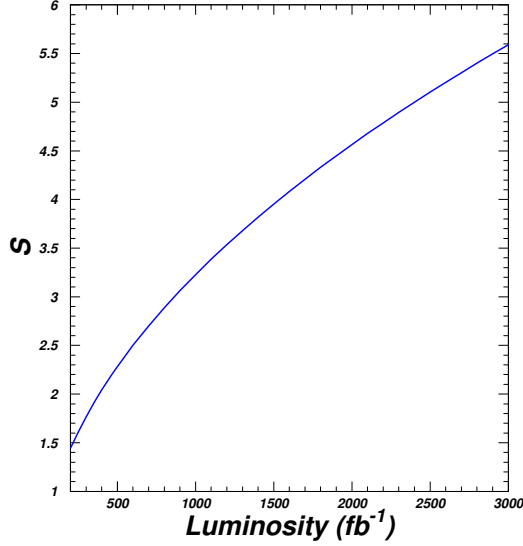


FIG. 7: The significance versus the integrated luminosity of the 14 TeV LHC for the benchmark point.

VI. CONCLUSION

In this paper we study the capability of LHC to test DM, Z' , and vector-like quark in a local $U(1)_{L_\mu-L_\tau}$ model in light of the $b \rightarrow s\mu^+\mu^-$ anomaly and the DM observables. We take $m_Q < 2$ TeV and $m_{X_R} < 2$ TeV, and find that the $b \rightarrow s\mu^+\mu^-$ anomaly and the DM observables favor $m_{X_I} < 350$ GeV and $m_{Z'} < 450$ GeV after imposing relevant constraints from theory and $b \rightarrow s$ flavor observables. The current searches for jets and missing transverse momentum at the 13 TeV LHC with 139 fb^{-1} integrated luminosity data exclude $m_Q < 1.7$ TeV. Finally, we propose a novel channel of probing these new particles at the high luminosity LHC via the QCD process $pp \rightarrow D\bar{D}$ or $pp \rightarrow U\bar{U}$ followed by the decay $D \rightarrow s(b)Z'X_I$ or $U \rightarrow u(c)Z'X_I$ and then $Z' \rightarrow \mu^+\mu^-$. Taking a benchmark point of $m_Q=1.93$ TeV $m_{Z'} = 170$ GeV, and $m_{X_I} = 145$ GeV, we perform a detailed Monte Carlo simulation, and find that such benchmark point can be accessible at the 14 TeV LHC with an integrated luminosity 3000 fb^{-1} .

Acknowledgment

We thank Biaofeng Hou for the helpful discussions. This work was supported by the National Natural Science Foundation of China under grant 11975013, 11775025, and by the Natural Science Foundation of Shandong province (ZR2017JL002 and ZR2017MA004).

- [1] R. Aaij et al. [LHCb Collaboration], Phys. Rev. Lett. **113**, (2014) 151601.
- [2] R. Aaij et al. [LHCb Collaboration], Phys. Rev. Lett. **122**, (2019) 191801.
- [3] R. Aaij et al. [LHCb Collaboration], JHEP **1708**, (2017) 055.
- [4] M. Prim (for the Belle Collaboration), arXiv:1904.02440.
- [5] A. Datta, J. Kumar, D. London, Phys. Lett. B **797**, (2019) 134858.
- [6] X. G. He, G. C. Joshi, H. Lew and R. R. Volkas, Phys. Rev. D **43**, (1991) 22–24.
- [7] A. Crivellin, G. D’Ambrosio and J. Heeck, Phys. Rev. Lett. **114**, (2015) 151801.
- [8] W. Altmannshofer, S. Gori, S. Profumo and F. S. Queiroz, JHEP **12**, (2016) 106.
- [9] C.-H. Chen and T. Nomura, Phys. Lett. B **777**, (2018) 420–427.
- [10] S. Baek, Phys. Lett. B **781**, (2018) 376–382.
- [11] W. Altmannshofer, S. Gori, M. Pospelov and I. Yavin, Phys. Rev. D **89**, (2014) 095033.
- [12] W. Altmannshofer and I. Yavin, Phys. Rev. D **92**, (2015) 075022.
- [13] P. Arnan, L. Hofer, F. Mescia and A. Crivellin, JHEP **04**, (2017) 043.
- [14] S. Singirala, S. Sahoo and R. Mohanta, Exploring dark matter, Phys. Rev. D **99**, (2019) 035042.
- [15] P. T. P. Hutaauruk, T. Nomura, H. Okada and Y. Orikasa, Phys. Rev. D **99**, (2019) 055041.
- [16] A. Biswas, A. Shaw, JHEP **05**, (2019) 165.
- [17] Z.-L. Han, R. Ding, S.-J. Lin, B. Zhu, Eur. Phys. Jour. C **79**, (2019) 1007.
- [18] A. S. Joshipura, N. Mahajan, K. M. Patel, JHEP **03**, (2020) 001.
- [19] L. Bian, H. M. Lee, C. B. Park, Eur. Phys. Jour. C **78**, 306; arXiv:2008.03629.
- [20] G. H. Duan, X. Fan, M. Frank, C. Han, J. M. Yang, Phys. Lett. B **789**, (2019) 54-58.
- [21] P. Ko, T. Nomura and H. Okada, Phys. Rev. D **95**, (2017) 111701.
- [22] D. Liu, J. Liu, C. E. M. Wagner, X.-P. Wang, JHEP **06**, (2018) 150.
- [23] S. Baek, JHEP **05**, (2019) 104.

- [24] W. Altmannshofer, S. Gori, M. Pospelov and I. Yavin, Phys. Rev. Lett. **113**, 091801 (2014).
- [25] Y. Amhis et al., arXiv:1612.07233.
- [26] M. Misiak et al., Phys. Rev. Lett. **114**, (2015) 221801.
- [27] G. Belanger, F. Boudjema, A. Pukhov, A. Semenov, Comput. Phys. Commun. **185**, 960-985 (2014).
- [28] A. Alloul et al., Comput. Phys. Commun. **185**, 2250 (2014).
- [29] Planck Collaboration, Astron. Astrophys. A **27**, 594 (2016).
- [30] E. Aprile et al. [XENON Collaboration], arXiv:1805.12562.
- [31] J. Alwall *et al.*, JHEP **1407**, (2014) 079.
- [32] P. Torrielli and S. Frixione, JHEP **1004**, (2010) 110.
- [33] J. de Favereau *et al.* [DELPHES 3 Collaboration], JHEP **1402**, (2014) 057.
- [34] D. Dercks, N. Desai, J. S. Kim, K. Rolbiecki, J. Tattersall and T. Weber, Comput. Phys. Commun. **221**, (2017) 383.
- [35] ATLAS Collaboration, ATLAS-CONF-2019-040.
- [36] M. Cacciari, G. P. Salam, G. Soyez, JHEP **0804** (2008) 063.
- [37] C. Lester and D. Summers, Phys. Lett. B **463**, 99 (1999).
- [38] A. Barr, C. Lester and P. Stephens, J. Phys. G **29**, 2343 (2003).
- [39] H.-C. Cheng, Z. Han, JHEP **12**, 063 (2008).